MORPHOLOGICAL EFFECTS ON THE PHYSICAL PROPERTIES OF $Rb_jCo_k[Fe(CN)_6]_l \cdot nH_2O$ PRUSSIAN BLUE ANALOGUES

By

KATHERINE ALICE SOMODI

A THESIS PRESENTED TO THE UNDERGRADUATE CHEMISTRY DEPARTMENT
OF THE UNIVERSITY OF FLORIDA IN PARTIAL FULFILLMENT
OF THE REQUIREMENTS FOR UPPER DIVISION HONORS

UNIVERSITY OF FLORIDA

2013

To Opus Coffee

ACKNOWLEDGMENTS

I would like to thank Matthew Andrus for inviting me into the group as a freshman, and Dr. Daniel Talham for giving me the chance to learn and work throughout my undergraduate experience. I appreciate the introduction to lab work that I received by Matthieu Dumont and Emily Pollard who helped hone my lab skills. I especially appreciate Matthew Andrus for working closely with me for the majority of my experience, and being a constant source for advice, encouragement, and knowledge through research, classes, and application processes. Thanks to Olivia Risset, Caue Ferrera and UF Major Analytical Instrumentation Center for TEM images and EDS data. I extremely appreciate the synthesis and materials help I garnered from Carissa Li and Olivia Risset. The Talham group members were a consistently helpful think tank, Corey Gross, Hao Liu, Divya Rajan, Akhil Ahir, Yichen Li, Allison Garnsey, Ashley Felts, and Carolyn Averback.

I would like to thank Dr. Khalil Abboud for XRD time and data in conjunction with Matthew Andrus.

Finally, my best friends who have supported and uplifted me: Kayla, Jessica, Rebecca, and my boyfriend Nicolas. My family has been a source of encouragement throughout life and this process, Gail, Daniel, and Daniel C. Somodi. The communities I have been a part of have played a role in who I am, my motivation, drive, and stress relief, for that the Gator Wesley Foundation and Warren Willis United Methodist Camp deserve recognition. Importantly, I praise God for this intricate world, science, and determination.

This work was supported, in part, by the NSF, Grant No. DMR-105581 (DRT).

TABLE OF CONTENTS

page

LIST OF ABBREVIATIONS

C	Carbon
CHN	Carbon hydrogen nitrogen
CN	Cyanide
Co	Cobalt
$CoCl_2 \cdot 6H2O$	Cobalt chloride hexahydride
CoFe	Cobalt hexacyanoferrate
Cr	Chromium
CTIST	Charge transfer induced spin transition
cm^{-1}	Inverse centimeter
Cu	Copper
EDS	Energy dispersive spectroscopy
fcc	Face centered cubic
Fe	Iron
FTIR or IR	Fourier Transform Infrared
H	Hydrogen
H_2O	Water
HS	High spin
HT	High temperature
G	Gram
K	Potassium or Kelvin
KBr	Potassium bromide
$K_3Cr(CN)_6$	Potassium hexacyanochromate
$K_3Fe(CN)_6$	Potassium hexacyanoferrate
Lb	Pound
LS	Low spin

LT	Low temperature
M	Molar
mg	Milligram
mm	Millimeter
mM	Millimolar
mL	Milliliter
mL/hr	Milliliters per hour
mmol	Millimole
N	Nitrogen
Ni	Nickel
$NiCl_2 \cdot 6H_2O$	Nickel chloride hexahydrate
NiCr	Nickel hexacyanochromate
nm	Nanometer
O	Oxygen
PBA	Prussian blue analogue
S	Spin
Rb	Rubidium
RbCl	Rubidium chloride
T	Temperature
TEM	Transmission electron microscopy
XRD	X-ray diffraction
Å	Angstrom
Δa	Change in lattice constant

λ	Wavelength
°	Degree
μm	Micron

Abstract of Thesis Presented to the Department of Chemistry
of the University of Florida

MORPHOLOGICAL EFFECTS ON PHYSICAL PROPERTES IN $Rb_jCo_k[Fe(CN)_6]_l{\cdot}nH_2O$ PRUSSIAN BLUE ANALOGUES

By

Katherine Alice Somodi

December 2013

Chair: Daniel Talham
Major: Biochemistry

Prussian blue analogues (PBA) are a class of coordination polymers some of which are known to exhibit stimuli switchable magnetism. The mechanism in which these PBA undergo a change in magnetization is through a Charge Transfer Induced Spin Transition (CTIST). Of the materials that exhibit a CTIST, the PBA Cobalt hexacyanoferrate (CoFe) is the most extensively studied example. Recently PBA heterostructures, pairing two different components in a single material, have emerged, herein CoFe and Nickel hexacyanochromate (NiCr) are paired. These heterostructures exhibit changes in structural properties compared to pure CoFe and NiCr materials.

We propose that the interface coupling between the two lattices induces strain, which leads to new structural behaviors. To better understand these behaviors we investigate a series of morphologies. At room temperature there does not appear to be significant strain at the interface due to the lattice mismatch. However when cooled through the thermal CTIST both the NiCr and CoFe lattices are strained. NiCr by itself does not undergo a CTIST but when coupled to a CoFe core the NiCr lattice parameter contraction is greater than that of a thermal contraction. The extent of this contraction minimized when the shell thickness is increased. Therefore in this study the effect of

strain is investigated by varying shell thickness. As the NiCr shell grows from 10 nm to 95 nm, the CTIST of CoFe is diminished and the NiCr bulk character dominates. The thinnest NiCr shell, 10 nm, exhibits the most strain, induced by the CoFe core, which has the dominating core characteristics. A decreasing lattice constant for CoFe illustrates this as the NiCr shell increases.

A second series where CoFe is the shell material encasing a NiCr core (inverse to the first series) were investigated. The CoFe shell can only undergo a complete CTIST when the shell thickness is 40 nm or greater. Thinner shells result in partially inhibited transitions. Even though the shell is undergoing a CTIST, the NiCr core does not exhibit strain. A third series of hollow CoFe particles are prepared to enable study of the air-surface interface and its influence on the CTIST. Hollow CoFe shells do not undergo a complete CTIST until the shells are 70 nm thick. The hollow CoFe particles that undergo a CTIST are about twice the thickness required to completely transition for inverse heterostructures. This suggests that surface and morphology of the particles influence the CTIST.

CHAPTER 1
INTRODUCTION

Prussian Blue Analogues

The past decades have seen an upswing in Prussian Blue Analogue (PBA) research, especially with respect to molecular magnetism, which has been observed in several systems including $ACo[Fe(CN)_6]$, $AMn[Fe(CN)_6]$, $ACo[Os(CN)_6]$. The cobalt hexacyanoferrate, $ACo[Fe(CN)_6]nH_2O$ (CoFe), was the first system reported to exhibit a thermal and light induced change in magnetization have been meticulously studied. External stimuli have an effect on the electronic properties, meaning that switching temperature, light, magnetism, change the electronic and structural make up. This change from high spin (HS) to low spin (LS), for example, is accompanied by a physical change or unit cell contraction. The change in magnetization results from a charge transfer induced spin transition (CTIST) from $Co^{(II)}$—N-C—$Fe^{(III)}$ to $Co^{(III)}$—N-C—$Fe^{(II)}$. The change is a result of the cobalt changing from high spin to low spin. [1-4] The ability to manipulate the electronic properties and the material itself leads to possible applications in medicine[22-25] and technology such as biosensors and batteries.[26-28]

PBA are indexed to a face-centered cubic unit cell formation with mixed transition metals bridged by cyanide. Typically the molecular formula is expressed by the following, $A_jM_k[M'(CN)_6]l\cdot nH_2O$, where A is an alkali metal, M is a divalent metal, and M' is a trivalent metal. To achieve charge balance, either alkali metals intercalate the cubic structure, or water fills cyanometallate vacancies in the lattice Figure 1-1. These limiting examples produce HS and LS trapped material in CoFe. In most circumstances, both alkali metals and water are part of the lattice, which results in a substoichiometric molecular formula. Studies have been done with the limiting molecular formulas, and at

intermediate stoichoimetries. It has been noted that the ligand field strength surrounding the Co ion is determined by the number of coordinated wanters.[6] When water completes the lattice coordination sites, it stabilizes the HS state due to a weaker ligand field strength. The cyanide bridge, which mediates the electron transfer for intermediate stoichometries, assists in the CTIST between the high and low spin states making the CoFe PBA a prime candidate for investigating the structural and magnetic properties. This PBA was first studied for its photoinduced magnetism.[1,5]

Cobalt Hexacyanoferrate Prussian Blue Analogues

In the case of CoFe PBA the photomagnetism is a result of the CTIST, from a high temperature phase and low temperature phase. The HT phase is mostly Co^{2+} HS sites while LT phase consists of Co^{3+}LS sites. When thermal energy is added or removed from the system the HS or LS states are stabilized, which also results in a structural change[7] The Co-N bond contracts with the decrease in temperature, as indicated by XRD data, with lattice constants (a) of 10.30 Å (HT) to 9.96 Å (LT).[8,9,10]

Multiple factors may tune the potential energy between the states, HS and LS. Altering the ligand field strength around the Co by experimenting with stoichiometry[6] and the vacancies in the lattice has been documented, as well as changing the alkali metal.[29] Temperature and light have also been notable stimuli for inducing the CTIST, therefore changing potential energy.[11-15] Above 200 K, the HT phase is typically favored, however when below 200 K the LT phase stabilized. Light can used to excite the material from LT to HT phase below 150 K and below 25 the HT phase is know to order ferrimagneticallly.[9,11] The thermal hysteresis that occurs in CoFe PBA is illustrated

in Figure 1-2 as a function of magnetic susceptibility.[6,12]. Due to the phase changes that are accompanied by electronic and structural changes, the CTIST has been studied in differing terms.[6,13] Heterostructures and hollow particles have become important for probing the effects that, not only light, temperature, and pressure have on the structure; but also the effect of morphology of the material and how the surface interface plays into phase changes.

Heterostructured Prussian Blue Analogues

Heterostructures are multicomponent materials, where in this case the core is a PBA particle, which provides a nucleation site for the growth of a PBA shell surrounding the core. These core-shell heterostructures are defined as core@shell. When PBA with different properties are combined into a single material, there abounds new ways for controlling structural and electronic properties.[14,15] Herein, two different materials, one that exhibits a CTIST and is photoactive while the second material does not have either property, are studied in combination providing different electronic and physical, structural properties. In addition to CoFe, the other material in these studies is Nickel hexacyanochromate (NiCr). Herein the size of the NiCr shell on the CoFe core is varied in thickness to probe the effect in the core@shell morphology. Then the thickness of a CoFe shell on a NiCr core is studied. Of particular interest are the chemical and physical property changes when coupled materials are induced to phase changes, which can be studied because the bulk properties of each component are known. When NiCr and CoFe are heterostructured, there is a photoinduced decrease in magnetization at LT, when the shell is large enough, and an increase in ordering temperature for the photoexcited magnetism.[14,15,16] The observation that the CoFe@NiCr material stays

photomagnetic at higher temperature, leads to a major research interest in these materials. The morphology effects of the CoFe@NiCr, NiCr@CoFe, and hollow CoFe are compared herein, the interface study is attempted but information is lacking as to the role of the surface on the particles.

Hollow Cobalt Hexacyanoferrate Prussian Blue Analogues

Recently hollow PBA particles have been reported.[17] Prussian blue analogue hollows are successfully synthesized using a sacrificial template, in this case another PBA, Manganese hexacyanoferrate (MnFe).[17-20] The PBA of interest forms a core@shell before becoming a hollow shell.

It has been reported that hollow CoFe particles do not undergo a CTIST The current rationale for these particles remaining in the HT phase is either a morphology or surface effect. It is our aim to investigate how the physical properties of these hollow CoFe particles change as the shell thickness increases.The hollows are essentially surface, which enables a study on surface effects and characterization of these primarily surface particles. The thickness of the hollow shell determines their ability to undergo a CTIST. At 10 nm, the thinnest shell, the particles are LS trapped; when grown larger, up to 70 nm, the shell begins to exhibit a fraction of the character of a core particle, in the ability to undergo a CTIST. Studying the thicknesses of these hollow shells can be taken as studying simply the surface of the PBA, in this case CoFe. When the heterostructured materials are studied and characterized, it is seen that the surface penetrates into the core, and that the core properties penetrate the shell. The hollows have no other material in coordination when washed properly, therefore, are able to

attribute strain or changes to the morphology of the particle. Herein the hollows are compared to heterostructures such that surface effects, size, and overall morphology can be characterized. The unique properties of the particles are attributed to their morphologies.

The particles are synthesized for careful cross comparison such that morphologies can be utilized to discover reasoning behind physical changes as a result of the CTIST. Heterostructures: CoFe@NiCr, inverse heterostructures: NiCr@CoFe, and Hollow CoFe can correlate the effects lattice coupling and morphology have on the physical properties of CoFe PBAs.

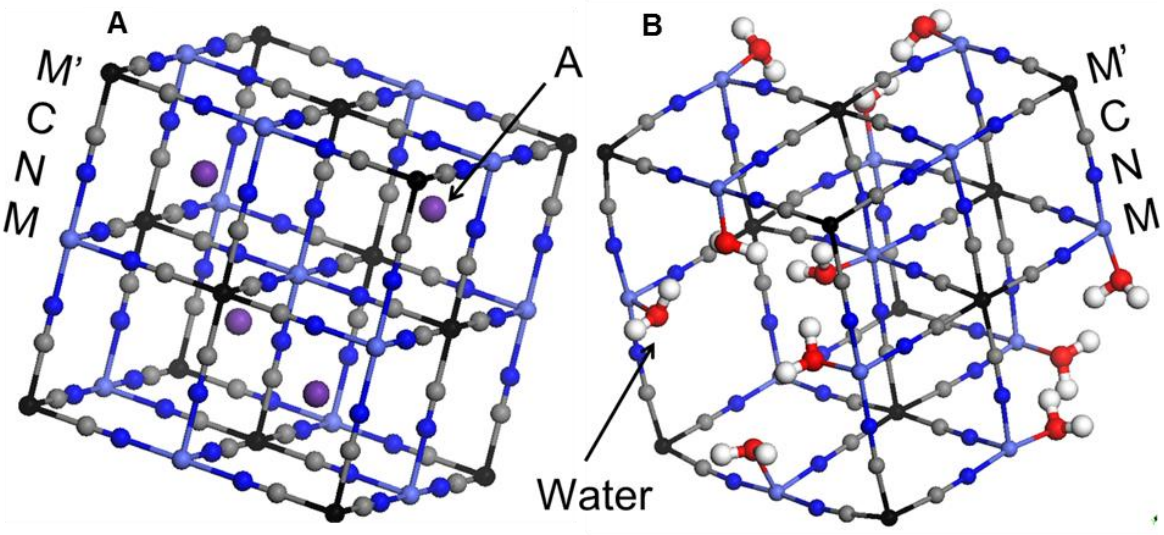

Figure 1-1. The limiting PBA unit cells. The left illustrates the alkali metal cationic charge balance, the right, when water coordinates to preserve charge balance.

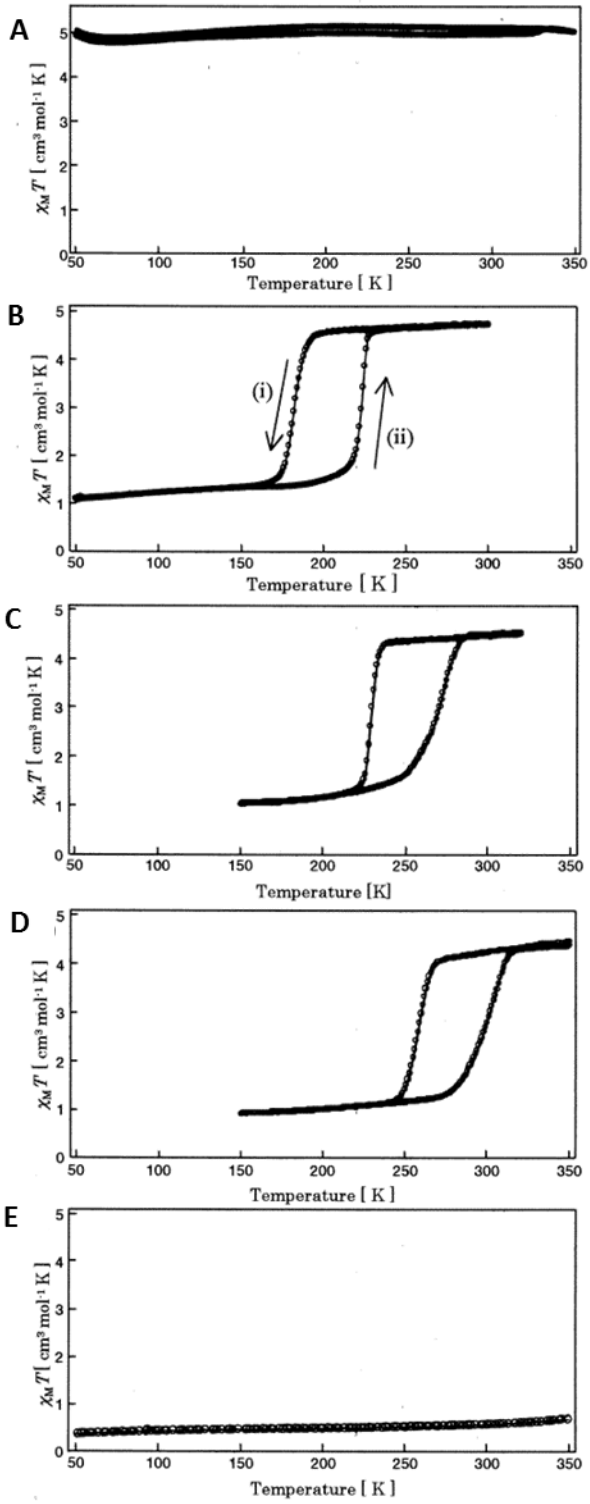

Figure 1-2. Magnetic susceptibility times temperature, versus temperature plots. Sodium, the alkali metal in this series of PBA, is varied and the CTIST is tuned. Reprinted with permission from Shimamoto, et al. copyright 2002 American Chemical Society.[6]

CHAPTER 2
MATERIALS AND METHODS

Reagents

All reagents were purchased from Sigma-Aldrich, Fisher, or Acros. $K_3Cr(CN)_6$ was synthesized by reacting aqueous potassium cyanide and chromium (III) chloride trihydrate in NANOpure water, recrystallizing in methanol.[30] Deionized water was used where indicated; the other following synthetic procedures utilized Barnstead NANOpure water with 17.2 Ω resistivity or above. All other reagents were not purified further from the manufacturer. The filters used were Fast Bottle Top Filters 0.45μm PES, Nalgene.

Bare RbCoFe Synthesis

The synthesis of the CoFe-PBA for core particles was performed at room temperature. In 200 mL of an aqueous solution containing $CoCl_2.6H_2O$ (95 mg; 0.40 mmol) and RbCl (95 mg; 0.79 mmol) were added dropwise (3.5 mL/min) to an equal volume of an aqueous solution containing $K_3[Fe(CN)_6]$ (150 mg; 0.46 mmol). After maturation for 4 hours under vigorous stirring, the particles were centrifuged at 9000 rpm for 10 min and subsequently washed with 300 mL of water. These core particles were prepared by Olivia Risset.

Sample 2-1 $Rb_{0.3}Co_{1.3}[Fe(CN)_6]\cdot nH_2O$. Particle Size 160 ± 20 nm. Purple powder. IR (KBr): 2159 cm^{-1} (ν_{CN}, Co^{II}-NC-Fe^{III} (HS)); 2113 cm^{-1} (ν_{CN}, Co^{II}-NC-Fe^{III} (LS)); 2094 cm^{-1} (ν_{CN}, Co^{II}-NC-Fe^{II}). EDS (Co/Fe) 48.70:36.22. Anal. Calcd for: C, 18.48; H, 3.08; N, 21.56. Found: C, 18.27; H, 2.12; N, 20.92.

RbCoFe@NiCr Core@Shells Synthesis

One half of the total volume of recovered CoFe core particles (Sample 2-1) were used

to grow the shells. Table 2-1 outlines the synthetics parameters used. X mg of $NiCl_2 \cdot 6H_2O$ and y mg of $K_3Cr(CN)_6$ were added to two separate Erlenmeyer flasks each with z mL of DI water. Simultaneously, each solution was added dropwise (3.5 mL/min) to a suspension containing w mL of DI water and half of the previously prepared sample. After maturation for 4 hours under vigorous stirring, the particles were centrifuged at 9000 rpm for 10 min and subsequently washed with 300 mL of water. Half of the redispersed suspension was dried under room temperature while the other half was used to synthesize the next shell thickness.

Sample 2-2 $Rb_{0.3}Co_{1.3}[Fe(CN)_6]\cdot nH_2O@K_{0.4}Ni_{1.3}[Cr(CN)_6]\cdot nH_2O$. Particle size 200 ± 20 nm. Purple powder. IR (KBr): 2159 cm^{-1} (ν_{CN}, Co^{II}-NC-Fe^{III} (HS)); 2113 cm^{-1} (ν_{CN}, Co^{II}-NC-Fe^{III} (LS)); 2094 cm^{-1} (ν_{CN}, Co^{II}-NC-Fe^{II}); 2174 cm^{-1} (ν_{CN}, Ni^{II}-NC-Cr^{III}). EDS (Co/Fe) 34.77:24.93; (Ni/Cr) 15.48:12.42.

Sample 2-3 $Rb_{0.3}Co_{1.3}[Fe(CN)_6]\cdot nH_2O@K_{0.4}Ni_{1.3}[Cr(CN)_6]\cdot nH_2O$. Particle size 240 ± 30 nm. Purple powder. IR (KBr): 2159 cm-1 (ν_{CN}, Co^{II}-NC-Fe^{III} (HS)); 2113 cm-1 (ν_{CN}, Co^{II}-NC-Fe^{III} (LS)); 2094 cm^{-1} (ν_{CN}, Co^{II}-NC-Fe^{II}); 2174 cm^{-1} (ν_{CN}, Ni^{II}-NC-Cr^{III}). EDS (Co/Fe) 25.32:19.09; (Ni/Cr) 24.28:21.00.

Sample 2-4 $Rb_{0.3}Co_{1.3}[Fe(CN)_6]\cdot nH_2O@K_{0.4}Ni_{1.3}[Cr(CN)_6]\cdot nH_2O$. Particle size 280 ± 20 nm. Purple powder. IR (KBr): 2159 cm^{-1} (ν_{CN}, Co^{II}-NC-Fe^{III} (HS)); 2113 cm^{-1} (ν_{CN}, Co^{II}-NC-Fe^{III} (LS)); 2094 cm^{-1} (ν_{CN}, Co^{II}-NC-Fe^{II}); 2174 cm^{-1} (ν_{CN}, Ni^{II}-NC-Cr^{III}). EDS (Co/Fe) 16.79:12.29; (Ni/Cr) 35.98:27.98.

Sample 2-5 $Rb_{0.3}Co_{1.3}[Fe(CN)_6]\cdot nH_2O@K_{0.4}Ni_{1.3}[Cr(CN)_6]\cdot nH_2O$. Particle size 350 ± 40 nm. Purple powder. IR (KBr): 2159 cm^{-1} (ν_{CN}, Co^{II}-NC-Fe^{III} (HS)); 2113 cm^{-1}

(v_{CN}, Co^{II}-NC-Fe^{III} (LS)); 2094 cm^{-1} (v_{CN}, Co^{II}-NC-Fe^{II}); 2174 cm^{-1} (v_{CN}, Ni^{II}-NC-Cr^{III}). EDS (Co/Fe) 10.79:7.53; (Ni/Cr) 42.35:32.01.

Bare NiCr Synthesis

The synthesis of the NiCr-PBA for core particles was performed at room temperature. A 150 mL aqueous solution of $NiCl_2 \cdot 6H_2O$ (0.6 mmol) and KCl (1.2 mmol), and a 150 mL aqueous solution of $K_3Cr(CN)_6$ (0.68 mmol) were simultaneously added dropwise to 300 mL of deionized water. The solution was kept under vigorous stirring for 20 hours after complete addition. The particles were subsequently filtered under vacuum using a 0.45 μm filter, then washed and dispersed with nanopure water. For collection and analysis, the particles were redispersed in a 50:50 solvent mixture of water and acetone and dried under room temperature. These samples were synthesized by Carissa H. Li.

Sample 2-6 $K_{0.4}Ni_{1.3}[Cr(CN)_6] \cdot nH_2O$. Particle Size 110 ± 10 nm. Green powder. IR (KBr): 2169 cm^{-1} (v_{CN}, Ni^{II}-NC-Cr^{III}); EDS (Ni/Cr) 54.51:42.65. Anal. Calcd for C4.4H3.2N4.4O1.6K0.4Ni1.4Cr: C, 20.37; H, 1.25; N, 23.76. Found: C, 16.793; H, 2.957; N, 18.995.

NiCr@RbCoFe Core@shells Synthesis

Table 2-1 details the concentrations used to grow the CoFe shells. In short, x mg of $CoCl_2 \cdot 6H_2O$ and y mg of $K_3Fe(CN)_6$ was added to two separate Erlenmeyer flasks each with z mL of DI water. Simultaneously, each solution was added dropwise (3.5 mL/min) to a suspension containing w mL of DI water and the core sample. After maturation for 4 hours under vigorous stirring, the particles were centrifuged at 9000 rpm for 10 min and subsequently washed with 300 mL of water. These samples were synthesized by Carissa H. Li using the Sample 2-6 as the NiCr core.

Sample 2-7 $K_{0.4}Ni_{1.3}[Cr(CN)_6]\cdot nH_2O@Rb_{0.4}Co_{1.3}[Fe(CN)_6]\cdot nH_2O$. Particle size 130 ± 10 nm. Purple powder. IR (KBr): 2174 cm^{-1} (v_{CN}, Ni^{II}-NC-Cr^{III}); 2159 cm^{-1} v_{CN}, Co^{II}-NC-Fe^{III} (HS)); 2113 cm^{-1} (v_{CN}, Co^{II}-NC-Fe^{III} (LS)); 2094 cm^{-1} (v_{CN}, Co^{II}-NC-Fe^{II}). EDS (Ni/Cr) 28.64:21.21; (Co/Fe) 23.13:18.06.

Sample 2-8 $K_{0.4}Ni_{1.3}[Cr(CN)_6]\cdot nH_2O@Rb_{0.4}Co_{1.3}[Fe(CN)_6]\cdot nH2O$.Particle size 160 ± 20 nm. Purple powder. IR (KBr): 2174 cm^{-1} (v_{CN}, Ni^{II}-NC-Cr^{III}); 2159 cm^{-1} (v_{CN}, Co^{II}-NC-Fe^{III} (HS)); 2113 cm^{-1} (v_{CN}, Co^{II}-NC-Fe^{III} (LS)); 2094 cm^{-1} (v_{CN}, Co^{II}-NC-Fe^{II}). EDS (Rb/Co/Fe) 5.74: 31.35: 22.77; (Co/Fe) 30.70:21.31.

Sample 2-9 $K_{0.4}Ni_{1.3}[Cr(CN)_6]\cdot nH_2O@Rb_{0.4}Co_{1.3}[Fe(CN)_6]\cdot nH_2O$. Particle size 190 ± 20 nm. Purple powder. IR (KBr): 2174 cm^{-1} (v_{CN}, Ni^{II}-NC-Cr^{III}); 2159 cm^{-1} (v_{CN}, Co^{II}-NC-Fe^{III} (HS)); 2113 cm^{-1} (v_{CN}, Co^{II}-NC-Fe^{III} (LS)); 2094 cm^{-1} (v_{CN}, Co^{II}-NC-Fe^{II}). EDS (Ni/Cr) 13.24:10.97; (Co/Fe) 37.53:27.52.

Hollow RbCoFe Synthesis

A 50 mL aqueous solution of 0.50 mmol $MnCl_2$ added, by peristaltic pump at 2.5 mL/min to an equal volume of aqueous 0.55 mmol $K_3[Fe(CN)_6]$ and 1.50 mmol RbCl. Particles were filtered in a 0.45 µm PES Nalgene filter after 4 hours of vigorous stirring. The particles were resuspended in 250 mL water/methanol (4:1) mixture.

The core@shell particles follow the Risset et al. method. Dissolved in 100 mL of water/methanol (4:1) are 0.42 mmol $CoCl_2*6H_2O$ and 0.83 mmol RbCl, and an equal solvent mixture containing 0.20 mmol $K_3[Fe(CN)_6]$ was added at 8 mL/h simultaneously to the core suspension of particles. This stirred vigorously overnight and was filtered under vacuum using the 0.45 µm PES filter.

The core@shells are sonicated and stirred in 1 L of 45 °C water for 45 minutes, thus becoming hollows. This suspension was filtered using a 0.45 μm filter and repeated twice. Following the final filtration the particles were dispersed in a minimum amount of water and a quarter portion air dried for the bare hollows analysis.

The hollow shells were grown further by adding a 100 mL aqueous solution of 0.35 mmol $CoCl_2$*$6H_2O$ and 0.58 mmol RbCl simultaneously with a 0.30 mmol $K_3[Fe(CN)_6]$ solution to an aqueous solution containing ¾ original product in 400 mL of DI water. The solution with an addition rate of approximately 8 mL/h, stirred vigorously overnight. The product was filtered, resuspended, and portioned such that 1/2 dried, while the remaining 1/2 repeated the same procedure to “grow” the hollows.

Sample 2-10 $Rb_{0.4}Co_4[Fe(CN)_6]_{2.8}\cdot nH_2O$. Particle size 70 ± 20 nm. Purple powder. IR (KBr): 2159 cm^{-1} (ν_{CN}, Co^{II}-NC-Fe^{III} (HS)); 2113 cm^{-1} (ν_{CN}, Co^{II}-NC-Fe^{III} (LS)); 2094 cm^{-1} (ν_{CN}, Co^{II}-NC-Fe^{II}); 2174 cm^{-1}. EDS (Co/Fe) 1.3.

Sample 2-11 $Rb_{0.7}Co_4[Fe(CN)_6]_{2.9}\cdot nH_2O$. Particle size 110 ± 20 nm. Purple powder. IR (KBr): 2159 cm^{-1} (ν_{CN}, Co^{II}-NC-Fe^{III} (HS)); 2113 cm^{-1} (ν_{CN}, Co^{II}-NC-Fe^{III} (LS)); 2094 cm^{-1} (ν_{CN}, Co^{II}-NC-Fe^{II}); 2174 cm^{-1}. EDS (Co/Fe) 1.3.

Sample 2-12 $Rb_{0.7}Co_4[Fe(CN)_6]_{2.9}\cdot nH_2O$. Particle size 150 ± 20 nm. Purple powder. IR (KBr): 2159 cm^{-1} (ν_{CN}, Co^{II}-NC-Fe^{III} (HS)); 2113 cm^{-1} (ν_{CN}, Co^{II}-NC-Fe^{III} (LS)); 2094 cm^{-1} (ν_{CN}, Co^{II}-NC-Fe^{II}); 2174 cm^{-1}. EDS (Co/Fe) 1.3.

Sample 2-13 $Rb_{0.7}Co_4[Fe(CN)_6]_{2.9}\cdot nH_2O$. Particle size 190 ± 20 nm. Purple powder. IR (KBr): 2159 cm^{-1} (ν_{CN}, Co^{II}-NC-Fe^{III} (HS)); 2113 cm^{-1} (ν_{CN}, Co^{II}-NC-Fe^{III} (LS)); 2094 cm^{-1} (ν_{CN}, Co^{II}-NC-Fe^{II}); 2174 cm^{-1}. EDS (Co/Fe) 1.3.

Characterization

Fourier-Transform Infrared Spectroscopy (IR) measurements were performed on a Thermo Scientific Nicolet 6700 spectrometer depositing <1 mg of sample on a KBr pellet. The measurements took place in the 1800-2500 cm^{-1} range with a 1 cm^{-1} resolution over 16 scans. Both Energy Dispersive X-Ray Spectroscopy (EDS) and Transition Electron Microscope (TEM) were conducted on the JEOL 2010F Field Transmission TEM at the Major Analytical Instrumentation Center at the University of Florida. Using water and acetone suspensions CoFe PBA samples were deposited onto a 400 mesh copper grid with ultrathin carbon film on a holey carbon support film, from Ted Pella, Inc. Particle size analysis was determined by measuring more than 150 particles' edge lengths were using ImageJ software.[31] Combustion analysis was performed at the University of Florida Spectroscopic Services Laboratory to determine carbon, hydrogen, and nitrogen (CHN) content.

Powder X-ray diffraction (XRD) measurements were performed on a Bruker DUO diffractomer using Cu K_α radiation from an IμS source, multi-layered mirror optics and an APEXII CCD area detector (1024 x 1024) at 150 mm from the sample. Samples were packed into capillary tubes, 0.3 mm in diameter, boron-rich and thin walled, from Charles Supper Company. Between 5° and 89°, diffraction patterns were collected, with a 600 s/image collection time. The temperature, cooling, was controlled by nitrogen gas flow, regulated by an Oxford Cryostream. APEXII generated the raw data and this was analyzed using Fullprof Rietveld refinement software.[21]

Table 2-1. The precursor quantities for the referenced samples.

Sample	x (mg)	y (mg)	z (mg)	w (mL)
2-2	48	75	50	400
2-3	33	53	35	350
2-4	33	53	35	250
2-5	19	30	20	200
2-7	23	35	50	400
2-8	45	69	50	400

CHAPTER 3
RESULTS AND DISCUSSION

Analysis of Heterostructure PBA

Three different PBA heterostructures were studies, CoFe@NiCr, NiCr@CoFe, and hollow CoFe. For a schematic on morphology see Figure 3-1. To determine the M^{2+}/M^{3+} ratio, EDS was conducted, as it identifies the elements and their relative abundance .The molecular formulas were determined by EDS and CHN; where the alkali metal content was determined by charge balance. FTIR was used to confirm the components of the heterostructures. Morphology and particle size was evaluated by TEM. Table 3-1, compiles the samples' particle size, shell size, and other important data. The TEM data can also be seen in Figures 3-2,4.

Powder X-Ray Diffraction (XRD)

The powder XRD measurements were important for determining the structure of the PBA coordination polymers. The unit cells for NiCr and CoFe were determined using Bragg's law, at 300 K and 100 K. Furthermore, broadening of the reflections can provide insight towards lattice strain. There are a couple of possibilities attributed to peak broadening such as non-stoichiometric ratios in the compound or lattice mistakes. Here anisotropic strain is the primary component of peak broadening, which is observed in the cooled, LT phase. Movement of the highest intensity peaks indicate contraction of the unit cell, which in CoFe, bare particles, is very common and results from the CTIST, slight changes in lattice constant for NiCr is also observed. (Table3-1)

The unit cells for NiCr and CoFe were indexed to a FCC lattice, using the 200, 220, 400, 420, reflections. The peak center was determined using a pseudo-Voigt fit. The reflections determine the unit cell length, which when compared between the high

and low temperatures can be used to indicate physical state changes. Figure 3-5 is a compilation of the diffraction pattersn for each sample in the HT and LT phases, A to B respectively. The full width at half maximum (FWHM) from the Viogt fit of the most intense reflections helps to determine broadening during cooling, a characteristic of strain. A change in the width of the peak can be compared on stacked plots and quantified; the causes of this are to follow.

Pure Bare PBA

The bare terminology implies that the material is not modified by heterostructure, or otherwise different morphology. The particles are in the FCC lattice. Their molecular formula, as listed in Chapter 2, is near identical to the other particles utilized for the study, thus is an ideal reference.

The particles used for this study were in the HT phase at 300 K. When cooled to 100 K the particles undergo a CTIST and the unit cell contracts to the LT phase. The unit cell contraction has a lattice constant, $\Delta a=0.35$Å**.** Pure CoFe sees broadening in the hk0 (i.e. 420) reflections at low temperature. NiCr does not undergo a CTIST, the XRD information illustrates this lack of phase change, see Table 3-1. The XRD data demonstrates this lack of phase change, though there is a subtle shift in the reflections which is attributed to thermal contraction.

The bare materials are a reference for the heterostructures and hollow particles to be compared. The aspects such as particle size were carefully constructed by synthetic techniques such as addition rate and stir time such that the sizes would be comparable and logical.

CoFe@NiCr Heterostructured PBA

The heterostructures were similarly studied. When cooled from 300 K to 100 K the CTIST appears to be inhibited to greater extents with increasing shell thickness. The 15 nm NiCr shell shows signs of strain, see Figure 3-5, sample 2-2, that are not typically present for NiCr. The lattice constant for the 15 nm NiCr shell sample decreases more than any other heterostructure or bare NiCr materials. In the 40 nm shell materials, there is less of a decrease in lattice constant for the NiCr shell, as seen in Table 3-1. Along with this is a a decreased lattice constant, meaning less of a contraction, for the CoFe core. The largest NiCr shell, has essentially overcome the strain imposed by the CoFe core, referencing Table 3-1, sample 2-5. The CoFe CTIST has been depleted as evidenced by the lattice constant. For CoFe@NiCr core@shells the size of the NiCr shell affected the extent to which the CTIST was able to occur in the CoFe. The CoFe/NiCr interface influences the extent to which both lattices contract when cooled to 100 K. If the shell thickness is small, the strain is quite apparent and the CTIST in CoFe is closer to the pure material CITST. The change in unit cell, a decrease, illustrates the CTIST associated physical change. Furthermore, for the thinnest NiCr shell at low temperature has a much smaller lattice parameter than the pure NiCr material. This suggests the change in CoFe lattice is influencing the shell material. Additionally, the hk0 reflections of NiCr shell are broadened; another indication of strain at the interface. This is measured by an increase in FWHM. The CoFe must influence the shell for the first several layers. It is asserted that a rigid NiCr shell inhibits the CTIST due to lattice coupling at the interface as the NiCr increases in thickness. The shell of 95 nm, approaching the size of the core particle, diminishes the CTIST. Though, it is not until

about 60 nm that the shell behaves like the pure NiCr material. Strain on NiCr decreases as the thickness of the shell increases.

NiCr@CoFe Heterostructured PBA

The NiCr@CoFe core@shell particles are an inverse system to the previous heterostructure samples and give the opportunity to further probe morphology effects. For this series CoFe is the shell material with thicknesses ranging from 10 to 40 nm. The thinnest CoFe shell (10 nm) does not undergo a CTIST. Two factors could be limiting this transitions, either the NiCr core inhibits the transition or the shell is so thin it acts purely as a surface and cannot undergo the CTIST. This study aims to better understand this inhibition. The ratio of the Co/Fe suggests that this shell should undergo a CTIST, however, the lattice coupling or surface effects prevent the phase change from happening. By increasing the CoFe shell thickness the material begins to undergo a CTIST. See Table 3-1, samples 2-7,8,9. As the shell thickness is increased to 40 nm a complete transition occurs. This suggests the morphology does not entirely inhibit the CTIST. However, it is unclear if the surface or the morphology inhibits the CTIST in the thinnest shell. This point will be discussed in more detail later on in this report. It is also important to note that the NiCr does not show evidence of strain, by comparison of FWHM during cooling of the inverse heterostructures. There is no significant change in the NiCr lattice parameter upon cooling to 100 K as observed in the CoFe@NiCr heterostructures. However, the CoFe shows evidence of strain possibly from the interface with NiCr and the particle surface. The complexity of this system makes it difficult to differentiate morphology and surface effects. Therefore, hollow CoFe particles were investigated to provide further insight into the source of strain on the CoFe shell.

Hollow CoFe PBA

The hollow CoFe PBA shells studied allow for possible determination of the source of strain in the heterostructure particles, as hollows serve as a prime example of possible surface strain. Four sets of hollow particles were grown with shell thickness ranging from 10 to 70 nm. The 10 nm CoFe hollow particles did not undergo a CTIST as previously reported in the literature. When increased in thickness, a lattice contraction occurs. However, the contraction is incomplete for hollow CoFe particles with shell thicknesses less than 70 nm. See Figure 3-5,7 for the hollow particle X-Ray diffraction patterns. Hollow particles require thicker shells than the NiCr@CoFe shells to undergo a complete CTIST. This strain could be attributed to the morphology of the hollow shell, simply being a shell, or having surface effects. From this study, the difference of strain origin is unclear. However analyzing the comparison morphologies could be enlightening.

The NiCr@CoFe particles undergo a complete CTIST when the shell thickness is 40 nm. Meanwhile, hollow CoFe particles need a thickness of 70 nm to undergo a complete CTIST. Despite having the same morphology the hollow particles need to be nearly twice as thick. This suggests that the hollow cubes are not flexible enough to go through the CTIST, which is an attribute of surface effects. Thereby increasing the shell thickness reduces the overall surface nature of the hollow particles and subsequently bulk properties begin to dominate. The fact that a CTIST is possible in a hollow morphology indicates that it is not the morphology itself preventing a CTIST in lower thicknesses. Compare the 2-13 sample to the smaller shell hollow particles' X-ray diffraction patterns, Figure 3-7. We assert that the surface, penetrating the few available

layers of the thin hollow shells, inhibit the CTIST. The surface, compared to larger thicknesses, has less ability to penetrate the shell and exhibit any control on the phase change or cell contraction. Several parameters still influence the CTIST. It is difficult to conclude completely and differentiate each effect. However, with these samples we can conclude different factors mediate the CTIST in CoFe PBA particles, heterostructures, and nanocubues through differences in surface, morphology and strain effects. This offers new insights into ways to tune these material properties.

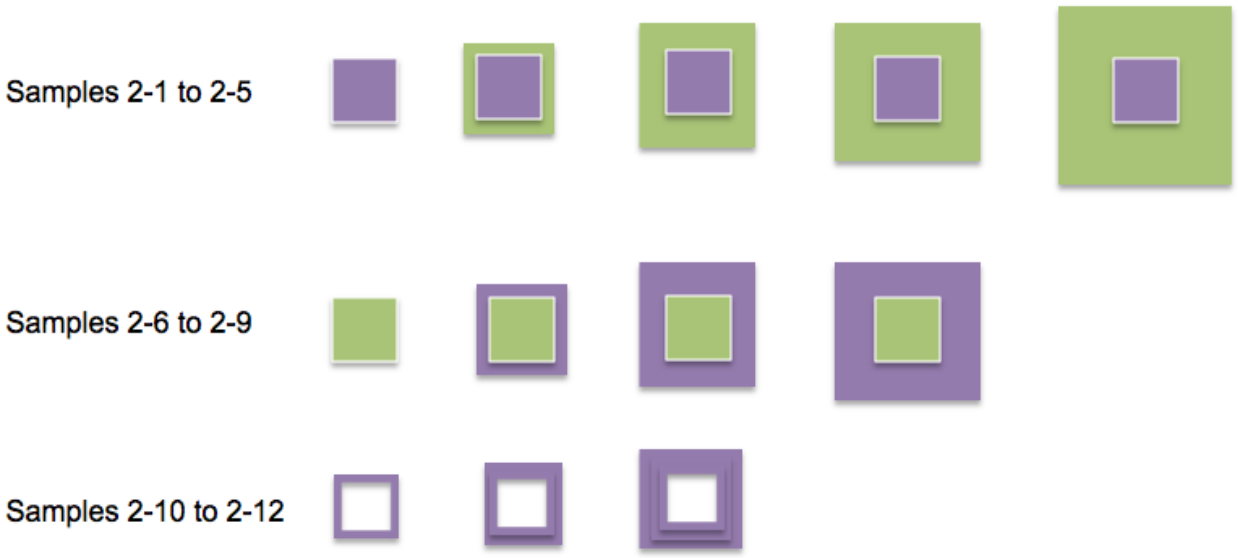

Figure 3-1. A schematic illustrating the morphology of the particles included in the study.

Table 3-1. The properties discussed for the samples mentioned throughout the document. Matthew J. Andrus obtained the XRD data.[21]

Sample	Core size (nm)	Shell thickness (nm)	Lattice Constants (Å) 300 K Core	300 K Shell	100 K Core	100 K Shell	Δa Core	Δa Shell
2-1	160±20	--	10.28	--	9.96	--	0.32	--
2-2	160±20	15	10.27	10.41	9.99	10.29	0.28	0.12
2-3	160±20	40	10.28	10.20	10.03	10.37	0.24	0.05
2-4	160±20	60	10.27	10.42	10.06	10.39	0.21	0.03
2-5	160±20	95	10.28	10.44	10.09	10.41	0.18	0.03
2-6	110±20	--	10.45	--	10.43	--	0.02	--
2-7	110±20	10	10.45	10.29	10.43	10.24	0.02	0.05
2-8	110±20	30	10.45	10.30	10.44	10.14	0.02	0.16
2-9	110±20	40	10.45	10.30	10.42	9.95	0.03	0.35
2-10	70±20	10	--	10.28	--	10.23	--	0.05
2-11	70±20	20	--	10.29	--	10.19	--	0.1
2-12	70±20	40	--	10.28	--	10.12	--	0.16
2-13	70±20	70	--	10.28	--	9.96	--	0.32

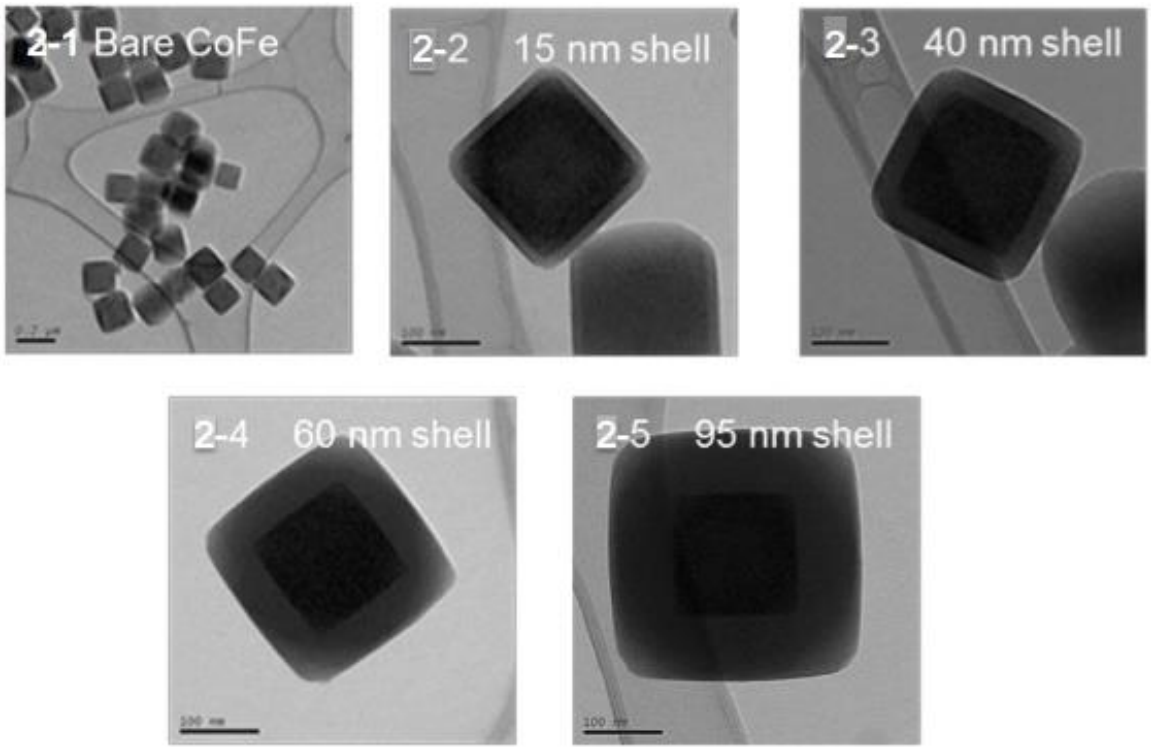

Figure 3-2. TEM images for the CoFe and CoFe@NiCr labeled by shell thickness.

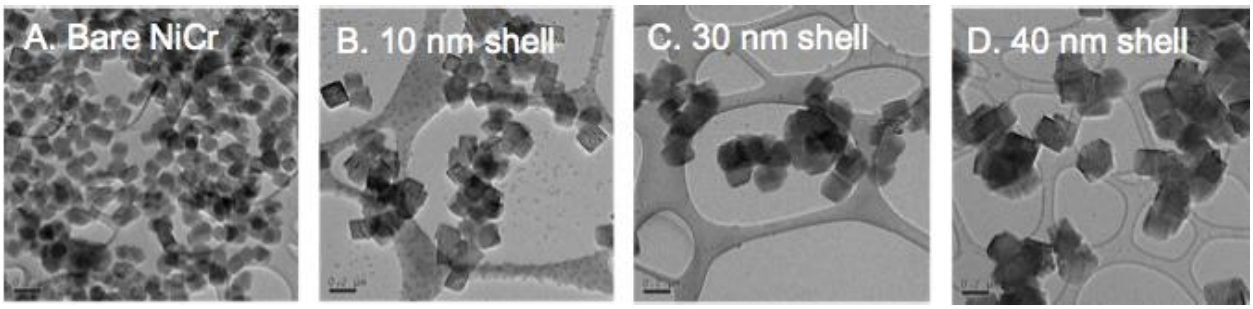

Figure 3-3. TEM images for the NiCr and NiCr@CoFe labeled by shell thickness. In order A-D, 2-6,9.

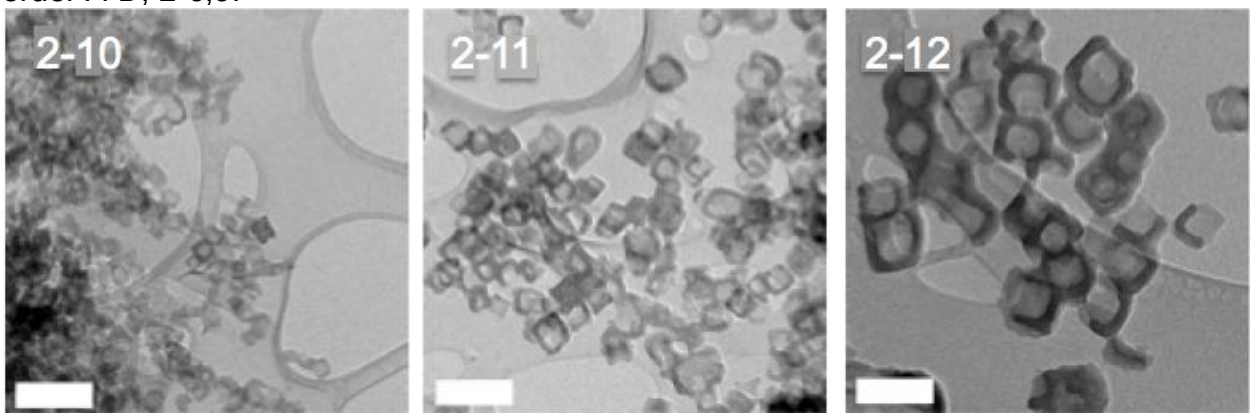

Figure 3-4. TEM images for Hollow RbCoFe.

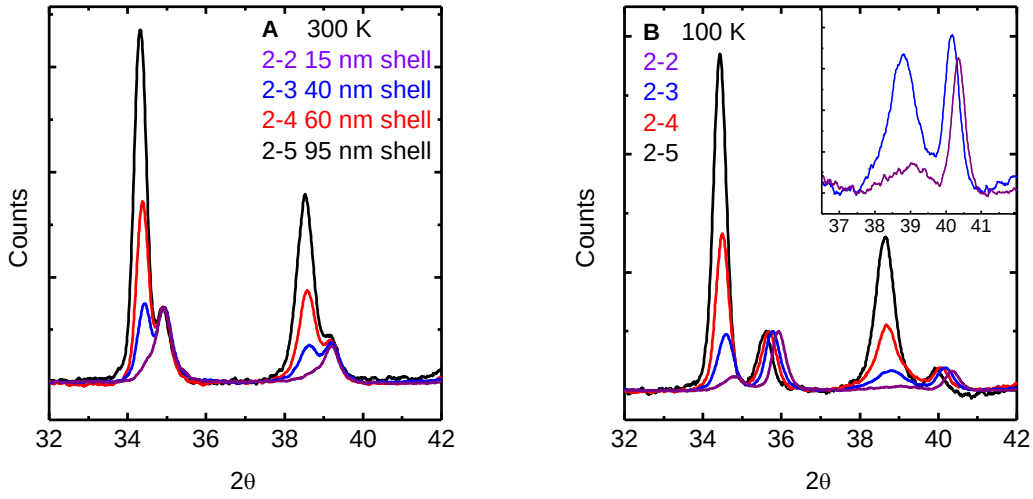

Figure 3-5. XRD data for CoFe@NiCr heterostructures, samples 2-2 – 2-5 are shown above.

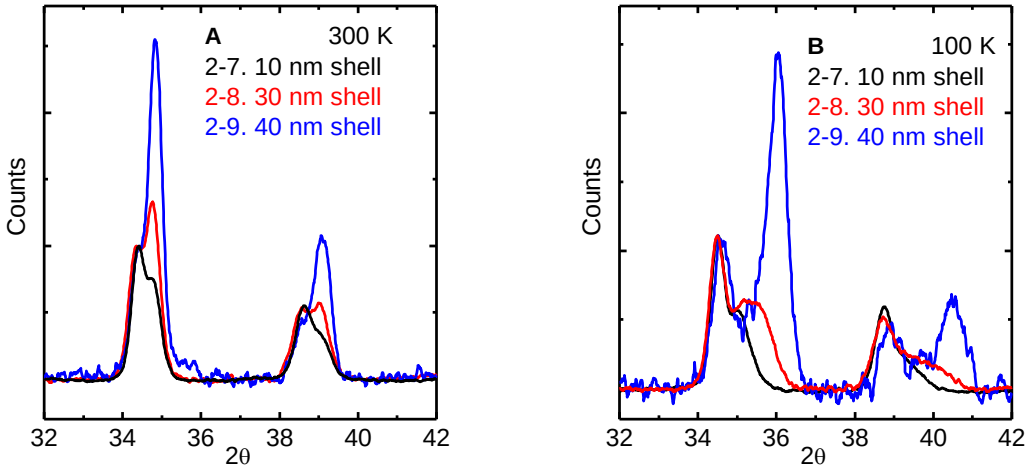

Figure 3-6. XRD for Inverse Heterostructures NiCr@CoFe, samples 2-7 - 2-9, 400 and 420 reflections are shown above.

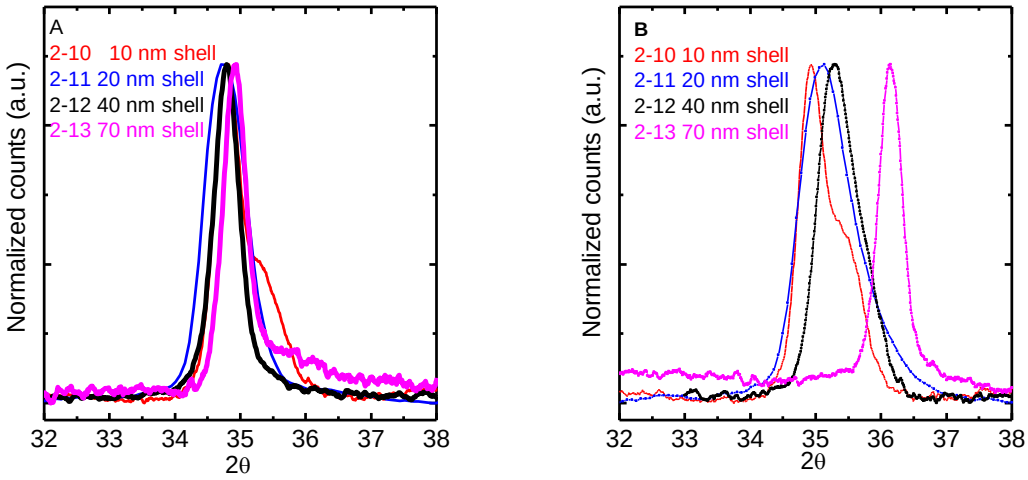

Figure 3-7. XRD data for the hollow samples, 2-10 – 2-13, the 400 reflection is shown above.

CHAPTER 4
CONCLUSIONS

The size, shape, and formation of the PBAs studied all have an effect on the physical properties of the material itself. Collectively, these morphology effects play into unit cell changes, phase behavior and photomagnetism. The strain on CoFe core@shell PBAs when undergoing a CTIST is more intense when CoFe is the core as opposed to when NiCr is the core. Hollows behave slightly differently from bulk CoFe or CoFe shell materials, in that they are spin trapped until thick enough to escape influence by a surface interface. The character of hollow particles is therefore not simply a question of their morphology, but of their surface effects. It has been found that at the interface of materials, especially in the core@shells, the properties are different and the strain on the material may be caused by this character difference. When the thickness of the shells or hollows grow, spin trapped states or strain decrease, as the original material character has a chance to predominate.

In the future, magnetic measurements must be done, such that the magnetic properties of the hollows, especially, may be compared to the known magnetic behavior of bulk, nano, and heterostructured materials. The XRD was able to study the unit cell changes or strain as the temperature induced HS to LS changes in materials. Alternatively important, would be to see the changes in magnetization as hollows undergo the CTIST, as the thinnest would be spin-trapped and the hollow particles above 70 nm may exhibit magnetization changes relatively similar to those observed in pure bare particles.

These measurements may be integral in determining the use of the surface area on hollows and ways to design materials according to phase or magnetic need or use.

LIST OF REFERENCES

[1] O. Sato, T. Iyoda, A. Fujishima, K. Hashimoto, Science 272 (1996) 704-705.

[2] M. Verdaguer Science 272 (1996) 698-699.

[3] C. Avendano, M. G. Hilfiger, A, Prosvirin, C. Sanders, D. Stepien, K. R. Dunbar, J Am. Chem. Soc. 132 (2010) 13124-13125.

[4] O. Sato, Y. Einaga, A. Fujishima, K. Hashimoto, Inorg. Chem. 38 (1999) 4405.

[5] K. Yoshizawa, F. Mohri, G. Nuspl, and T. Yamabe, J. Phys. Chem. B 102 (1998) 5432-5437.

[6] N. Shimamoto, S-I. Ohkoshi, O. Sato, K. Hashimoto Inorg. Chem. 41 (2002) 678

[7] M. Kabir, K. Van Vliet, Phys Rev. B 85 (2012) 054431.

[8] M. Hanawa, Y. Moritomo, A. Kuriki, J. Tateishi, K. Kato, M. Takata, M. Sakata, J. Phys. Soc. Jap. 72 (2003) 987-990.

[9] A. Bleuzen, C. Lomenech, V. Escax, F. Villain, F. Varret, C. C. D. Moulin, M. Verdaguer, J. Am. Chem. Soc. 122 (2000) 6653-6658.

[10] O. Sato, Y, Einaga, T. Iyoda, A. Fujishima, K. Hashimoto, J. Phys. Chem. B 100 (1997) 3903.

[11] S. Ohkoshi, N. Machida, Z. J. Zhong, K. Hashimoto, Synth. Met. 122 (2001) 523–527.

[12] S. Ohkoshi, S.Ikeda, T. Hozumi, T. Kashiwagi, K. Hashimoto, J. Am. Chem. Soc. 128 (2006) 5320– 5321.

[13] J.-H. Park, F. A. Frye, N. E. Anderson, D. M. Pajeroswki, Y. D. Huh, D. R. Talham, M. W. Meisel, J. Magn. Magn. Mater. 310 (2007) 1458-145.

[14] D.M. Pajerowski, J.E. Gardner, F.A. Frye, M.J. Andrus, M.F. Dumont, E.S. Knowles, M.W. Meisel, D.R. Talham. Chem. Mater. 23 (2011) 3045-3053.

[15] M.F. Dumont, E.S. Knowles, A. Guiet, D.M. Pajerowski, A. Gomez, S.W. Kycia, M.W. Meisel, D.R, Talham. Inorg. Chem. 50 (2011) 4295-4300.

[16] H. Tokoro, T. Matsuda, T. Nuida, Y. Moritomo, K.; Ohoyama, E. D.; Loutete-Dangui, K. Boukheddaden, S. Ohkoshi, Chem. Mater. 20 (2008) 423– 428.

[17] O.N. Risset, E.S. Knowles, S. Ma, M.W. Meisel, D.R. Talham. Chem. Mater. 25 (2013) 42-47.

[18] Y. Zhu, J. Shi, W. Shen, X. Dong, J. Feng, M. Ruan, Y. Li. Angew. Chem. Int. Ed. 44 (2005) 5083-5087.

[19] Zhao, Y.; Jiang, L. Adv. Mater. 21 (2009) 3621−3638.

[20] A. Bleuzen, V. Marvaud, C. Mathoniere, B. Sieklucka, M. Verdaguer, Inorg. Chem. 48 (2009) 3453–3466.

[21] Andrus, M. J. Doctorate Dissertation, University of Florida, Gainesville, FL, 2013.

[22] Pearce, J. *Food and chemical toxicology* 32 (1994) 577.

[23] Heydlauf, H. *European journal of pharmacology* 6 (1969) 340.

[24] Hoffman, R. S.; Hoffman, R.; Stringer, J. A.; Feinberg, R. S.; Goldfrank, L. R. *Clinical Toxicology* 37 (1999) 833.

[25] Nelson, L. *Goldfrank's toxicologic emergencies*; McGraw-Hill Medical New York, 2011.

[26] Asakura, D.; Li, C. H.; Mizuno, Y.; Okubo, M.; Zhou, H. S.; Talham, D. R. *J Am Chem Soc* 135 (2013) 2793.

[27] Karyakin, A. A. *Electroanalysis* 13 (2001) 813.

[28] Ricci, F.; Palleschi, G. *Biosensors and Bioelectronics* 21 (2005) 389.

[29] Cafun, J. D.; Champion, G.; Arrio, M. A.; Moulin, C. C. D.; Bleuzen, A. *J Am Chem Soc* 132 (2010) 11552.

[30] Bigelow, J. H. *Inorg. Synth.* 2 (1946) 203.

[31] Rasband, W. S.; ImageJ, U. S. National Institutes of Health, http://imagej.nih.gov/ij/: Bethesda, Maryland, USA, 1997-2012.

BIOGRAPHICAL SKETCH

Katherine Somodi was born in Sarasota, Florida, and after a brief stint in North Carolina in elementary school, was raised in Bradenton, Florida. She attended Lakewood Ranch High School where she was class Vice President and salutatorian. She will be graduating with a Bachelor of Science in Biochemistry from the University of Florida.

Upon graduation she will continue volunteering at Helping Hands Clinic, as an eligibility specialist in an administration role, facilitating the provision of health care to homeless, uninsured, and impoverished in Gainesville. She will also continue to work as a barista at Opus Café. She will be regaining a role in The Vagina Monologues, Gainesville 2014, benefitting Peaceful Paths.

In her free time, Katherine enjoys rock climbing, heights, and outdoor adventures; such as zip lining on a volcano in Costa Rica. She has enjoyed the view of Machu Picchu from Wayna Picchu in Peru and the beauty of Lake Balaton in Hungary.

In the year to come she will be matriculating to medical school in pursuit of her life-long dream of being a doctor.